Photoacoustic guided ultrasound wavefront shaping for targeted acousto-optic imaging

Jacob Staley, Erwin Hondebrink, Wilma Peterson, and Wiendelt Steenbergen*

Biomedical Photonic Imaging Group, MIRA Institute for Biomedical Technology and Technical Medicine, University of Twente, P.O. Box 217, 7500 AE Enschede, Netherlands

**w.steenbergen@utwente.nl*

Abstract: To overcome speed of sound aberrations that negatively impact the acoustic focus in acousto-optic imaging, received photoacoustic signals are used to guide the formation of ultrasound wavefronts to compensate for acoustic inhomogeneities. Photoacoustic point sources composed of gold and superparamagnetic iron oxide nanoparticles are used to generate acoustic waves that acoustically probe the medium as they propagate to the detector. By utilizing cross-correlation techniques with the received photoacoustic signal, transmitted ultrasound wavefronts compensate for the aberration, allowing for optimized and configurable ultrasound transmission to targeted locations. It is demonstrated that utilizing a portable commercially available ultrasound system using customized software, photoacoustic guided ultrasound wavefront shaping for targeted acousto-optic imaging is robust in the presence of large, highly attenuating acoustic aberration.

OCIS codes: (170.1065) Acousto-optics; (110.5125) Photoacoustics; (170.7170) Ultrasound.

References and links

1. S. G. Resink, A. C. Boccara, and W. Steenbergen, "State-of-the art of acousto-optic sensing and imaging of turbid media," J. Biomed. Opt. **17**(4), 040901 (2012).
2. L. V. Wang and S. Hu, "Photoacoustic tomography: In vivo imaging from organelles to organs," Science **335**(6075), 1458–1462 (2012).
3. M. E. Anderson, M. S. McKeag, and G. E. Trahey, "The impact of sound speed errors on medical ultrasound imaging," J. Acoust. Soc. Am. **107**(6), 3540–3548 (2000).
4. P. D. Freiburger, D. C. Sullivan, B. H. LeBlanc, S. W. Smith, and G. E. Trahey, "Two dimensional ultrasonic beam distortion in the breast: in vivo measurements and effects," Ultrason. Imaging **14**(4), 398–414 (1992).
5. L. M. Hinkelman, D. L. Liu, R. C. Waag, Q. Zhu, and B. D. Steinberg, "Measurement and correction of ultrasonic pulse distortion produced by the human breast," J. Acoust. Soc. Am. **97**(3), 1958–1969 (1995).
6. G. Kossoff, E. K. Fry, and J. Jellins, "Average velocity of ultrasound in the human female breast," J. Acoust. Soc. Am. **53**(6), 1730–1736 (1973).
7. G. E. Trahey, P. D. Freiburger, G. Ng, and D. C. Sullivan, "The impact of acoustic velocity variations on target detectability in ultrasonic images of the breast," Invest. Radiol. **26**(9), 782–791 (1991).
8. G. E. Trahey, P. D. Freiburger, L. F. Nock, and D. C. Sullivan, "In vivo measurements of ultrasonic beam distortion in the breast," Ultrason. Imaging **13**(1), 71–90 (1991).
9. V. Behar, "Techniques for phase correction in coherent ultrasound imaging systems," Ultrasonics **39**(9), 603–610 (2002).
10. E. Bossy, K. Daoudi, A.-C. Boccara, M. Tanter, J.-F. Aubry, G. Montaldo, and M. Fink, "Time reversal of photoacoustic waves," Appl. Phys. Lett. **89**(18), 184108 (2006).
11. D. Cassereau and M. Fink, "Time-reversal of ultrasonic fields. III. Theory of the closed time-reversal cavity," IEEE Trans. Ultrason. Ferroelectr. Freq. Control **39**(5), 579–592 (1992).
12. M. Fink, "Time reversal of ultrasonic fields. I. Basic principles," IEEE Trans. Ultrason. Ferroelectr. Freq. Control **39**(5), 555–566 (1992).
13. X. Jin and L. V. Wang, "Thermoacoustic tomography with correction for acoustic speed variations," Phys. Med. Biol. **51**(24), 6437–6448 (2006).
14. J. Jose, R. G. Willemink, W. Steenbergen, C. H. Slump, T. G. van Leeuwen, and S. Manohar, "Speed-of-sound compensated photoacoustic tomography for accurate imaging," Med. Phys. **39**(12), 7262–7271 (2012).
15. R. Mallart and M. Fink, "Adaptive focusing in scattering media through sound-speed inhomogeneities - the Vancittert-Zernike approach and focusing criterion," J. Acoust. Soc. Am. **96**(6), 3721–3732 (1994).

#196549 - $15.00 USD Received 27 Aug 2013; revised 30 Oct 2013; accepted 20 Nov 2013; published 5 Dec 2013

16. S. E. Måsøy, T. F. Johansen, and B. Angelsen, "Correction of ultrasonic wave aberration with a time delay and amplitude filter," J. Acoust. Soc. Am. **113**(4), 2009–2020 (2003).
17. M. Tabei, T. D. Mast, and R. C. Waag, "Simulation of ultrasonic focus aberration and correction through human tissue," J. Acoust. Soc. Am. **113**(2), 1166–1176 (2003).
18. F. Wu, J. L. Thomas, and M. Fink, "Time reversal of ultrasonic fields. Il. Experimental results," IEEE Trans. Ultrason. Ferroelectr. Freq. Control **39**(5), 567–578 (1992).
19. K. Daoudi, A. Hussain, E. Hondebrink, and W. Steenbergen, "Correcting photoacoustic signals for fluence variations using acousto-optic modulation," Opt. Express **20**(13), 14117–14129 (2012).
20. D. J. Grootendorst, R. M. Fratila, M. Visscher, B. T. Haken, R. J. A. van Wezel, S. Rottenberg, W. Steenbergen, S. Manohar, and T. J. M. Ruers, "Intra-operative ex vivo photoacoustic nodal staging in a rat model using a clinical superparamagnetic iron oxide nanoparticle dispersion," J. Biophotonics **6**(6–7), 493–504 (2013).
21. D. J. Grootendorst, J. Jose, R. M. Fratila, M. Visscher, A. H. Velders, B. Ten Haken, T. G. Van Leeuwen, W. Steenbergen, S. Manohar, and T. J. Ruers, "Evaluation of superparamagnetic iron oxide nanoparticles (Endorem®) as a photoacoustic contrast agent for intra-operative nodal staging," Contrast Media Mol. Imaging **8**(1), 83–91 (2013).
22. S. Manohar, C. Ungureanu, and T. G. Van Leeuwen, "Gold nanorods as molecular contrast agents in photoacoustic imaging: the promises and the caveats," Contrast Media Mol. Imaging **6**(5), 389–400 (2011).
23. C. Ungureanu, R. Kroes, W. Petersen, T. A. M. Groothuis, F. Ungureanu, H. Janssen, F. W. B. van Leeuwen, R. P. H. Kooyman, S. Manohar, and T. G. van Leeuwen, "Light interactions with gold nanorods and cells: Implications for photothermal nanotherapeutics," Nano Lett. **11**(5), 1887–1894 (2011).
24. G. C. Ng, P. D. Freiburger, W. F. Walker, and G. E. Trahey, "A speckle target adaptive imaging technique in the presence of distributed aberrations," IEEE Trans. Ultrason. Ferroelectr. Freq. Control **44**(1), 140–151 (1997).
25. S. W. Flax and M. O'Donnell, "Phase-aberration correction using signals from point reflectors and diffuse scatterers: Basic principles," IEEE Trans. Ultrason. Ferroelectr. Freq. Control **35**(6), 758–767 (1988).

1. Introduction

In recent years there have been great advances in employing optical techniques for biomedically relevant applications. However, due to the high optical scattering of biological tissue, the depth of purely optical techniques has been relegated to superficial layers – typically a few optical mean free paths. To overcome this limitation photoacoustic (PA) and acousto-optic (AO) imaging modalities have been employed with great success [1, 2]. PA imaging techniques rely on the interaction of pulsed laser light with optical absorbers (endogenous or exogenous) to generate acoustic waves that are received by broadband ultrasound detectors. By relying on acoustic detection of optically generated signals, PA imaging mitigates the disadvantages of purely optical techniques, which mainly arise from the reduction in acoustic scattering compared to optical scattering. AO techniques also combine aspects of sound and light, albeit with different fundamental mechanisms. AO imaging relies on the detection of modulated diffused light by creating an ultrasound focus, commonly referred to as a "tagging volume", that induces phase shifts in light that passes through this tagging region. Localized pressure changes in the tagging volume create particle displacements and spatially varying refractive index values that are dictated by the ultrasound frequency and peak pressure amplitudes. This interaction between diffuse light and tagging volume provides localized optical contrast at acoustic focus resolution.

Biological tissue has been shown to have a destructive effect on ultrasound focusing behavior, primarily from the spatial variation in speed of sound (SOS) values when looking at soft tissue [3–8]. This creates a detrimental effect in AO imaging due to the requisite of a well formed tagging volume for localized modulation of diffused light. There has been a large amount of research dedicated to formulating techniques to compensate for acoustic aberrations arising from speed of sound inhomogeneities [5, 9–18]. Recently our group has shown the ability of AO to fluence compensate PA imaging through the combination of AO and PA techniques [19]. The issue remains how to account for distortion of the acoustic focus and target desired locations to perform AO fluence compensation of PA in an acoustically inhomogeneous medium. To overcome SOS aberrations of the acoustic focus we employ PA signals to acoustically probe the medium between the point of PA source generation and a linear phased ultrasound detector array. The acoustic variations are inscribed in the PA waves as they propagate through the medium and are subsequently accounted for by cross-correlating received signals to extract appropriate delays. The delays obtained from the cross-

#196549 - $15.00 USD Received 27 Aug 2013; revised 30 Oct 2013; accepted 20 Nov 2013; published 5 Dec 2013

correlation procedure are used to return a compensated ultrasound wavefront back to the source of the PA signal allowing for a targeted and SOS compensated AO measurement. The benefit of using a cross-correlation technique, as opposed to a strictly time-reversed signal, is the control of the frequency, amplitude and size (i.e. ultrasound pulse-duration) of the tagging volume, which is essential due to the low signal-to-noise ratio often obtained with AO imaging.

In this work we experimentally demonstrate PA guided ultrasound wavefront shaping (PUWS) to perform targeted AO measurements in highly optical diffuse tissue phantoms in the presence of a large acoustic defocusing slab, as well as an acoustically heterogeneous pork tissue sample. The PA signals are generated by exogenous contrast agents (gold nanospheres (GNS), gold nanorods (GNR) and superparamagnetic iron oxide nanoparticles (SPIOs)), which have been chosen for their applicability with PA biomedical applications [20–23]. Compensated ultrasound wavefronts are formed via a programmable commercial ultrasound system and AO measurements are made using pulsed-wave ultrasound and stroboscopic illumination with parallel speckle detection via a CCD camera.

2. Materials and methods

2.1 Photoacoustic contrast agents

Three PA contrast agents were used for the targeted AO measurements – GNS (60 nm diameter), GNR (aspect ratio ~2.5) and SPIOs (Sienna + ®, EndoMagnetics, Cambridge, United Kingdom). A sodium alginate solution (1.5-2.0%) contained the given contrast agent. The solution was pipetted into a 0.7M working stock of $CaCl_2$. By varying the size of the pipette tip and height at which the sodium alginate and contrast agent solution is deposited into the $CaCl_2$, it is possible to control the size and shape of the resulting bead. The bead diameter was shown to be controllable between 1 and 5 mm.

Absorption spectrum measurements of the GNS, GNR and SPIOs were made and the results are seen in Fig. 1. The GNS (Fig. 1(a)) had a peak absorption of 535 nm, while the GNR (Fig. 1(a)) exhibited a peak absorption (longitudinal resonance) of 714 nm. The SPIOs absorption spectrum is more broadband when compared to GNS and GNR, and decays with increasing wavelength as seen in Fig. 1(b).

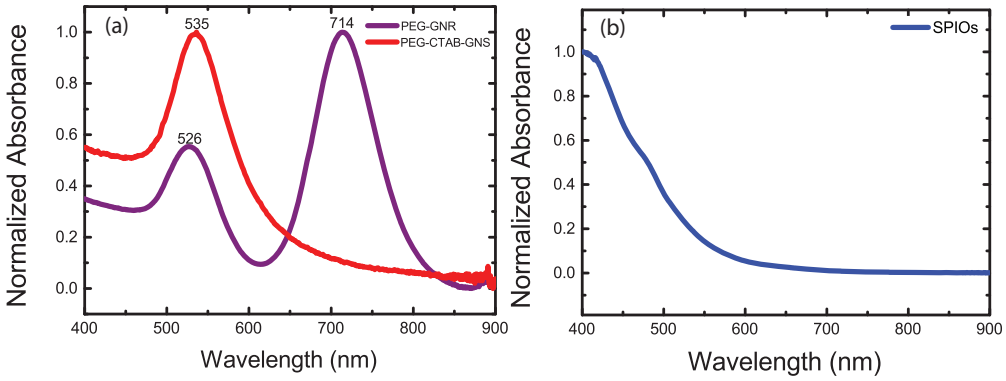

Fig. 1. Normalized absorption spectrum of the photoacoustic contrast agents. (a) Absorption spectrum of the gold nanospheres and gold nanorods. (b) Absorption spectrum of SPIOs.

It should be noted that we expect a slight red shift in the absorption spectrum of the contrast agents when they reside in the sodium alginate beads.

2.2 Photoacoustic guided ultrasound

A near field phase screen model creates aberrations in the ultrasound wave by applying a thin aberrating layer on the transducer surface. The aberrating layer's effect is to introduce time

#196549 - $15.00 USD Received 27 Aug 2013; revised 30 Oct 2013; accepted 20 Nov 2013; published 5 Dec 2013

shifts of the transmitted and received acoustic waves on individual transducer probe elements of the linear phased array. Assuming geometrical path length differences for signal arrival times across probe elements have been taken into account, delays introduced by the aberrating screen (neglecting attenuation) can be expressed as:

$$p_i(t) = s\left(t-\tau_i\right) \tag{1}$$

where τ_i is the time shift from encountering the phase screen, $p_i(t)$ is the detected pressure at an array element from the PA signal $s(t)$, generated from a PA point source. We can express Eq. (1) in terms of linear tilts on the phase spectra of PA signals received on individual array elements from the shift theorem of Fourier Transforms by:

$$\begin{aligned} &\mathcal{F}\left\{s(t-\tau_i)\right\} = P_{aber,i} = S(f)\exp[-j2\pi f\tau_i], \\ &S(f) = \mathcal{F}\left\{s(t)\right\} \end{aligned} \tag{2}$$

which states that a delay τ_i creates a linear phase shift of $2\pi f\tau_i$ radians of the phase spectrum, while preserving the magnitude spectra of the detected complex signal $P_{aber,i}$ over the time period $t = z/c$, where c is the speed of sound and z is the axial distance between the ultrasound detector and the PA point source [24]. Using cross-correlation techniques the individual time shifts between received PA signals at adjacent probe elements can be accurately estimated from [9]:

$$Corr_{i,i+1}(k) = \sum_{m=-M/2}^{M/2-1} P_{aber,i}(mT_S)P^*_{aber,i+1}((m+k)T_S) \tag{3}$$

where M is the number of signal samples over the sampling time interval T_s. Adding a compensating time shift maximizes the cross-correlation and removes the relative phase difference between spectra at the adjacent signals, ignoring any attenuation. The relative delays between $P_{aber,i}$ and $P_{aber,i+1}$ are found at the offset (k_o) that produces a peak in the cross-correlation of Eq. (3), which is $\Delta\tau_{i,i+1} = k_oT_s$. Iterating through all elements and performing the cross-correlation results in the widely known neighbor-element technique proposed by Flax and O'Donnel [25]. Extending the neighbor-element technique to use a central element from which all subsequent relative delays are calculated was numerically shown to perform better in noisy data sets [9]. By choosing a central element from which all others are phase corrected eliminates the phase error that is accumulated across the elements of the ultrasound array in the neighbor-element approach. The central element technique is described by:

$$\begin{aligned} &Corr_i(k) = \sum_{m=-M/2}^{M/2-1} P_{aber,n+1}(mT_S)P^*_{aber,i}((m+k)T_S), \\ &i=1,\ldots,n,n+2,\ldots,N \end{aligned} \tag{4}$$

where $P_{aber,n+1}$ is the aberrated PA signal received at the central element, which is used as the reference signal, and N is the total number of ultrasound transducers in the array. This results in the relative delay for ultrasound array element i with respect to the central element, $\Delta_{\tau_i,n+1} = k_iT_s$. Repeating this process for all array elements produces a 1-D vector of time-delays $D_{\tau_{aber}} = [\tau_{aber,i}]i = 1,\ldots,N$ composed of photoacoustically probed speed of sound variations. To remove any outliers and eliminate the possibility of non-convergence of Eq. (4)

#196549 - $15.00 USD Received 27 Aug 2013; revised 30 Oct 2013; accepted 20 Nov 2013; published 5 Dec 2013

in highly attenuating regions, $D_{\tau_{aber}}$ undergoes a robust locally weighted smoothing. After smoothing, the delays for shaping the ultrasound wavefront are applied to the corresponding ultrasound array elements for transmission.

2.3 Hydrophone measurement of ultrasound focus

A schematic diagram of the experimental setup for measuring the acoustic focus is shown in Fig. 2. Hydrophone measurements were made for comparing the ultrasound focusing ability of a fixed focus approach (i.e. traditional geometric beamforming) and the PUWS approach, with and without the phase screen attached to the ultrasound array. A nylon thread of diameter 230 μm was submerged in a water tank and suspended parallel to the elevation plane of the ultrasound array. A needle hydrophone (Precision Acoustics, 0.5mm diameter) was placed at the same height as the nylon thread.

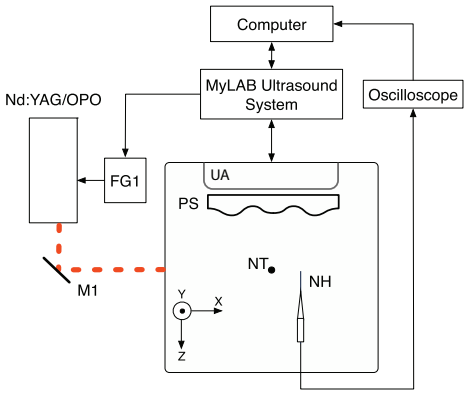

Fig. 2. Diagram of hydrophone measured ultrasound focus experimental setup. UA: ultrasound array, PS: phase screen, NT: nylon thread, NH: needle hydrophone, FG1: function generator: M1: mirror.

For PA measurements a frequency-doubled *Q*-switched Nd:YAG laser (10 Hz, 5ns pulse width) with an optional NIR wavelength from an optical parametric oscillator (OPO) was used to excite the nylon thread. PA signals were obtained from the thread by a portable commercial ultrasound system (MyLabONE, ESAOTE) using an 128-element ultrasound array (64 active elements per transmission/receive) with a central frequency of 7.5 MHz (model SL3323), provided with the MyLabONE system. The MyLabONE is configurable to run and switch between the provided commercial software, and the custom software that has been created for the PA guided focusing, through a software flashing process. Triggering of the laser was initiated by the ultrasound system through the use of a function generator, which synchronized the delay between flashlamp, *Q*-switch and PA acquisition. PA signals were acquired with and without the phase screen. The near-field phase screen is composed of silicone with an estimated speed-of-sound of ~1,000 m/s. The surface of the phase screen is smooth and irregular along the elevation plane as seen in Fig. 2. The ultrasound array was centered over the nylon thread, which was verified by observing arrival times of PA and ultrasound signals across the ultrasound array elements. The distance between the nylon thread and the ultrasound array was measured via depth analysis software on the MyLabONE and confirmed by the non-aberrated PA signal. The corresponding fixed focus to target the appropriate depth was applied to the ultrasound beam and scanned across the needle hydrophone. Similarly, the PA guided focus was scanned across the needle hydrophone. Scanning was achieved by using a LabVIEW controlled linear XY stage (MTS50-Z8, Thorlabs). Maps of the acoustic focus were collected via an oscilloscope (Textronix TDS 220), with and without the phase screen for both focusing techniques, and data was transferred to a computer for processing.

#196549 - $15.00 USD Received 27 Aug 2013; revised 30 Oct 2013; accepted 20 Nov 2013; published 5 Dec 2013

2.4 Photoacoustic and acousto-optic setup

AO measurements where undertaken using a stroboscopic parallel speckle transmission detection scheme as depicted in Fig. 3. Light at a wavelength of 532 nm from a single mode laser (Verdi, Coherent) passed through an acousto-optic-modulator (AOM), which was driven by FG2 and triggered by the ultrasound system. A LabVIEW program was responsible for setting the duty cycle of FG2, which dictated the optical pulse width exiting from the AOM. Delays in the duty cycle of FG2, based upon the trigger from the ultrasound system, allowed the ultrasound to propagate (z-axis in Fig. 3) configurable distances before interrogating the tagging volume with light. The pulse duration of the ultrasound coincided with the pulse duration of the light. The synchronization of both pulsed ultrasound and light transmission allows for axial resolution along the ultrasound transmission axis. To increase the SNR, ultrasound and light pulses were sent into the medium at a duty cycle of 12.5 kHz. The resulting speckle images were captured by a CCD camera (Point Grey, Grasshopper 14S5M-C) with an integration time ranging from 2 to 10 ms. The change in speckle contrast (ΔC) was calculated at runtime by subtracting the contrast obtained from consecutive speckle images – one under insonification and the other without.

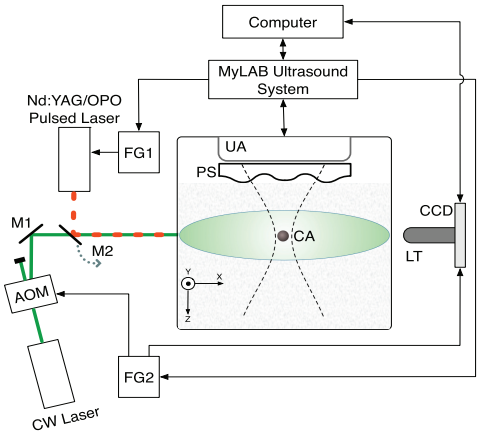

Fig. 3. Schematic of the PA and AO experimental setup. UA: ultrasound array, PS: phase screen, CA: contrast agent, FG1,FG2: function generator, AOM: acousto-optic modulator, M1: mirror, M2: flipping mirror, LT: lens tube.

For each experiment a single sodium alginate bead containing a PA contrast agent(s) was embedded in the medium. Two types of mediums were used in the experiments – an agar phantom made of 3% agar and 3% intralipid (20% concentration) and a 1.5x3.0x3.0 cm piece of pork tissue. The ultrasound array was fixed in place for each PA measurement and PA signals were recorded with and without the presence of the phase screen for the agar phantoms. The phase screen was not present during the pork tissue measurements due to the innate acoustic heterogeneities of the sample. When using gold nanoparticles the optical wavelength used for PA measurements was chosen to coincide with the peak absorption wavelength. Specifically, 532nm was selected for GNS and 720 nm for GNR. Wavelengths of 532, 720 and 780 nm were used with SPIOs due to their available broad absorption spectrum. The depth of each bead was calculated from the non-aberrated PA signal and verified with the ultrasound system's diagnostic capabilities for experiments dealing with tissue phantoms, and the incision location and PA signal was used for the pork tissue. To compare the performance of using unguided and PA guided focus in the presence of SOS aberrations, AO measurements with and without the phase screen were made in tissue phantom experiments using both ultrasound transmission focusing modes. No external aberration (i.e. phase screen) was present during the similar pork tissue experiments.

#196549 - $15.00 USD Received 27 Aug 2013; revised 30 Oct 2013; accepted 20 Nov 2013; published 5 Dec 2013

3. Results and discussion

The resulting focus profiles recorded by horizontally scanning the ultrasound array across the needle hydrophone are seen in Fig. 4(a) and 4(b). The phase screen is firmly attached to the ultrasound array as it moves during horizontal displacement. In Fig. 4(a) we see that the unguided and the PA guided focus, in the absence of the phase screen, are highly correlated, which is expected from a homogenous SOS distribution. However, in Fig. 4(b) there is a stark difference in the focusing behavior between the two techniques due to the introduction of the phase screen. The PA guided method accurately accounts for the delays induced by the phase screen, whereas the unguided case blindly transmits a wavefront with delays only compensating for geometrical distance differences across the ultrasound array, which are used to target the supplied depth. Comparing the focus profiles produced in Fig. 4(a) and 4(b) it is apparent that using the PA guided method it is possible to regain accurate focusing with minimal distortion despite large acoustic SOS variations and attenuation induced by the phase screen.

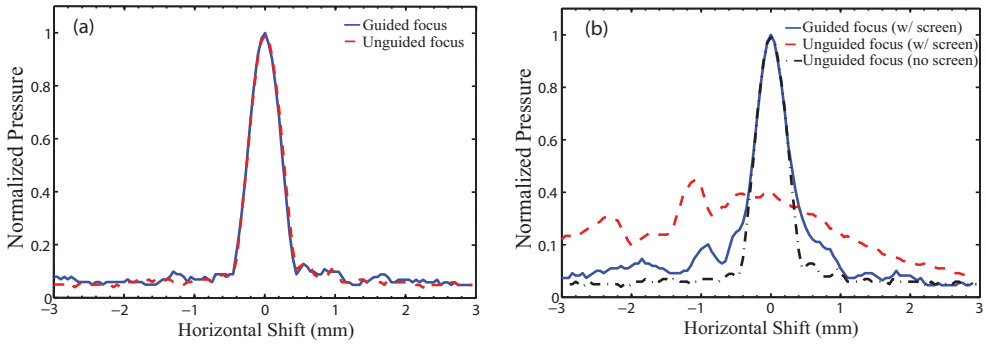

Fig. 4. The maximum signal amplitude (normalized relative to PA guided focus) as a function of scanning distance across the hydrophone. (a) Focus profile generated by the unguided (red) and PA guided focus (blue) without phase screen. (b) Focus profile generated by unguided (red) and PA guided focus (blue) with phase screen, and unguided focus without phase screen (black) as reference.

Figure 5 shows the normalized (maximum value) one-dimensional AO image (z-axis in Fig. 3) obtained from both ultrasound focusing techniques and their performance, with and without the phase screen attached to the ultrasound array. PA signals were obtained as discussed in sect. 2.4, and pulsed ultrasound wavefronts were sent to the 2 mm diameter sodium alginate bead containing GNS during illumination by the coherent laser source. In the absence of the phase screen the resulting AO measurement is nearly identical for both ultrasound transmission techniques, which is demonstrated by comparing the PA guided (blue) and unguided focus (red) plots in Fig. 5. This is the expected behavior due to the reproduction of highly correlated focal delays and resulting focus profiles for an acoustically homogenous medium. However, application of the phase screen to the ultrasound array introduces unaccounted aberrations to the unguided ultrasound wavefront, which negatively impacts the acoustic focus and detection of local optical contrast (black), whereas the PA guided method (green) is able to accurately reproduce the intended focus and performs similar to the non-aberrated cases. Further in Fig. 5, the localized dip in the peak of the ΔC occurring at ~23 mm is explained by the proper overlap of the ultrasound focus and the bead containing GNS. Light that would have normally been modulated by the ultrasound focus in the absence of the bead is now absorbed by the contrast agent, leading to the reduction of modulated diffuse light (light that has passed through the ultrasound focus). One can conclude that the ultrasound focus has reached its peak pressure (i.e. focus) at the location of the bead, and that the dip arises due to the local optical absorption from the contrast agent

#196549 - $15.00 USD Received 27 Aug 2013; revised 30 Oct 2013; accepted 20 Nov 2013; published 5 Dec 2013

and not from the loss of acoustic focus. Conversely in Fig. 5, the divergence of the fixed focus signal (black) from the others in the presence of the phase screen can be attributed to the loss of acoustic focus and a spatial redistribution of the acoustic energy to a region that is no longer confined to the area occupied by the bead.

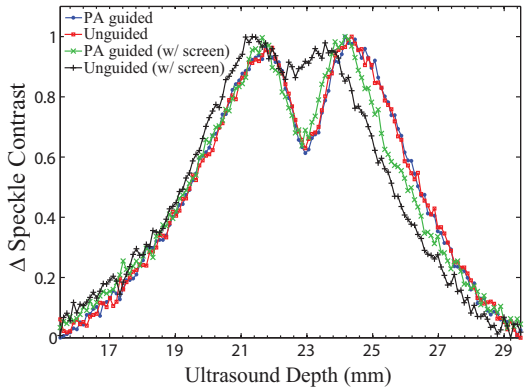

Fig. 5. Normalized AO measurement using unguided and PA guided ultrasound focus targeting a 2mm diameter bead of gold nanospheres. ΔC from unguided focus (red) and PA guided focus (blue) without phase screen. ΔC from unguided focus (black) and PA guided focus (green) in the presence of the phase screen.

Figure 6 highlights the ability to form a targeted ultrasound wavefront from a PA measurement by optically selecting the preferred gold nanoparticle based on its absorption spectrum. Figure 6(a) was created by optically targeting the GNR in a 1 mm diameter sodium alginate bead to form the PA guided focus, and performing the AO measurement by optically targeting the dominating absorption of the GNS contained within the same bead. The PA signal was generated at a wavelength of 720 nm to closely match the absorption peak of the GNR, and the AO measurement was performed at 532 nm to target the GNS, and to a lesser extent the latitudinal resonance of the GNR. These measurements were repeated with the phase screen attached for comparison of the focusing techniques. In Fig. 6(a), the depth between 30 and 31 mm contains a large reduction in ΔC arising from the absorption of light by the GNS + GNR present in the bead. The local dip occurs at the apex of the modulated signal, again verifying the overlap of the PA guided focus and bead. This trend is present with and without the use of the phase screen, which further shows the ability of PUWS to compensate for speed of sound aberrations. Figure 6(b) is the result of targeting a 2 mm diameter sodium alginate bead composed of SPIOs. The PA signal was generated using 720 nm wavelength and the resulting AO measurement was undertaken at a wavelength of 532 nm. For comparison, this was repeated with the phase screen attached to the ultrasound array. Again one can see that as the PA guided ultrasound focus converges towards the bead there is an increase in ΔC, which is a result of the local pressure increase, similar to the aforementioned experiments. Near the apex a sudden drop in the ΔC occurs at approximately 26-28 mm due to the presence of SPIOs in the bead. This is present with and without the use of the phase screen.

#196549 - $15.00 USD Received 27 Aug 2013; revised 30 Oct 2013; accepted 20 Nov 2013; published 5 Dec 2013

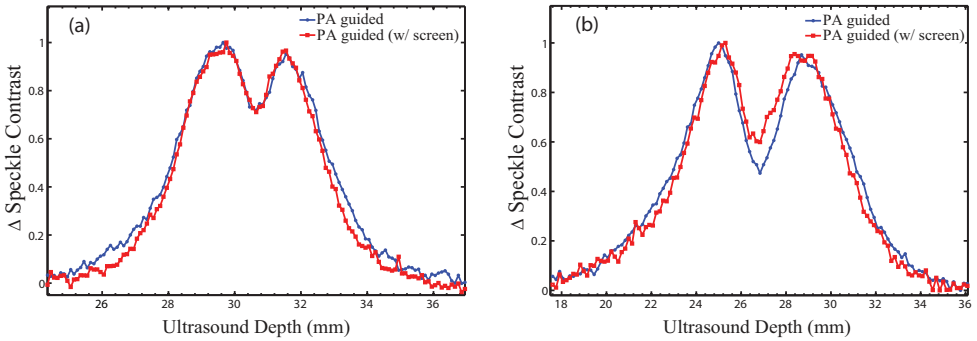

Fig. 6. Normalized AO measurement targeting a sodium alginate bead containing PA contrast agent(s). (a) 1 mm diameter bead containing GNS and GNR, (blue) ΔC from PA guided focus without phase screen, and (red) ΔC from PA guided focus with phase screen. (b) 2mm diameter bead containing SPIOs, (blue) ΔC from PA guided focus without phase screen, and (red) ΔC from PA guided focus with phase screen.

The anatomical, ultrasound and AO image from a heterogeneous piece of pork tissue is shown in Fig. 7. The dimensions of the tissue are approximately 1.5x3.0x3.0 cm along the x, y and z-axis, respectively. A 1 mm diameter sodium alginate bead containing SPIOs was embedded, via a small incision, approximately 7-8 mm deep in the tissue along the optical axis (x-axis), and approximately 15 mm along the y and z-axis as shown by the inset rulers in Fig. 7(a). This resulted in the bead residing approximately in the center of the tissue. The tissue sample was suspended in ultrasound gel for acoustic coupling and resided in the tissue holder used in the experiment as shown in Fig. 7(a). Once the ultrasound array had been centered above the bead, based upon the incision location, the ultrasound probe was fixed firmly in place. PA and AO measurements were made using 532 nm wavelength, without the presence of any external acoustic aberration (i.e. phase screen).

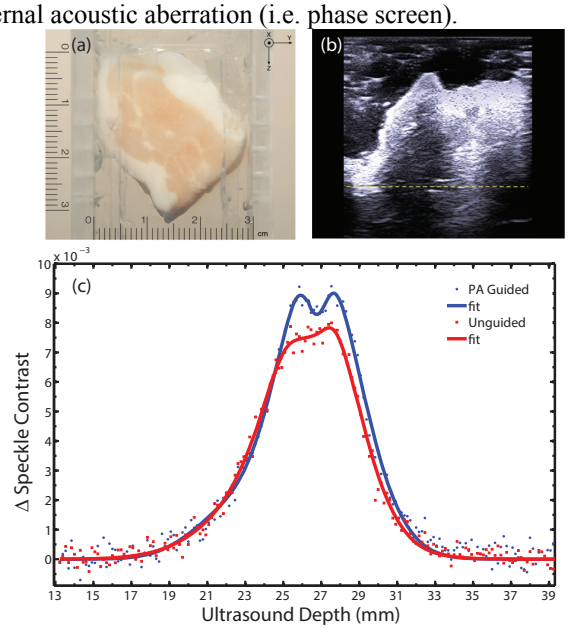

Fig. 7. Anatomical, ultrasound and AO image highlighting the heterogeneity of the pork tissue sample and the impact acoustic variations have on ultrasound and AO imaging. (a) 1.5x3.0x3.0 cm pork sample containing a 1 mm diameter sodium alginate bead composed of SPIOs embedded in the middle of the sample. (b) Ultrasound B-mode image of the sample after the ultrasound probe was aligned and fixed in position. (c) ΔC comparison from PA guided and unguided ultrasound focus used in the AO measurements.

#196549 - $15.00 USD Received 27 Aug 2013; revised 30 Oct 2013; accepted 20 Nov 2013; published 5 Dec 2013

As seen in Fig. 7(b), due to the presence of acoustic inhomogeneities (fat, muscle, connective tissue, etc.) in the tissue sample, the clarity of the resulting ultrasound image suffers considerably. This can be attributed to the spatial variation in the medium parameters (SOS, density, attenuation, etc.), which alters both the shape and position of the ultrasound beam focus during the ultrasound scan and the resulting B-mode image. From the ultrasound image alone the spatial location of the embedded bead is indiscernible, which leaves one blindly guessing as to where to focus ultrasound for making an AO measurement. However, using a-priori knowledge it is possible to set a geometric focus (i.e. no PA guidance) to target the bead. Based on the incision location, as well as the arrival time data from the PA signal, the ultrasound focal depth was set to 26.9 mm, which resides just below the yellow horizontal line in Fig. 7(b). The PA guided focus was calculated using the aforementioned process and the delays were applied to the ultrasound array for generating the targeted ultrasound wavefront. The results from the unguided and PA guided AO measurement are presented in Fig. 7(c).

After applying a fit to both data sets the improvement gained by PA guidance, over the unguided case, is clearly visible. The bead is resolved in the PA guided case (blue curve, Fig. 7(c)), which can be seen from the local dip in ΔC occurring at the ultrasound depth of ~26-27 mm. However, the unguided focus (red curve, Fig. 7(c)) fails to produce the same localized dip and suffers from a reduction in measured ΔC. This reduction in ΔC and lack of resolution can mainly be attributed to the degradation of a proper focus reaching the bead by assuming a homogenous SOS distribution. It should be noted that, even when using the a-priori information available (incision location, PA arrival time data) to center the probe and form an unguided focus, inevitably the alignment procedure for the unguided case in the pork tissue experiment is not exact. Any inaccuracy in the alignment procedure has the potential to impact the unguided result. With this in mind, the validity for having a guided ultrasound focus when making targeted AO measurements is further strengthened.

3. Conclusions

We have demonstrated the ability to use biomedically viable photoacoustic contrast agents to guide the formation of ultrasound wavefronts that self-target the generating source. It has been shown that using phase-aberration compensation techniques in conjunction with photoacoustic guidance allows for targeted acousto-optic imaging in the face of large and attenuating acoustic variations, as well as acoustic heterogeneities found in biological tissue. Further, with the ability to correct for SOS variations and target ultrasound to localized regions that are optically selected by the PA generating light source and absorption peak of the exogenous contrast agent(s), new avenues for further research are opened. For instance, interesting applications would be exploiting targeted delivery of PA contrast agents to newly developing tumors and using our technique to localize AO measurements to the cancerous region. This would be beneficial when insufficient acoustic contrast is obtained in traditional ultrasound imaging to guide the location of the AO measurement. Also, assuming the time to form the PA guided ultrasound focus is reduced, which is currently limited by the repetition rate of the pulsed laser in the system, our technique could be used to accommodate for mild motion artifacts (i.e. respiration in an animal model) when performing targeted AO imaging. Specifically, this would enable the ultrasound focus to follow the displacement of the PA contrast agent(s) bound to a region of interest (e.g. a tumor). Lastly, the natural extension of this work is the ability to fluence compensate PA imaging using AO in acoustically inhomogeneous media through the combined approach developed in our group [19].

Acknowledgments

We would like to acknowledge the collaboration of ESAOTE and their engineers for the help and discussion provided for the MyLabONE, as well as Khalid Daoudi for the insightful discussions. This research was supported by the Technology Foundation in the Netherlands (STW) under vici-grant 10831, and by the MIRA Institute of the University of Twente.

#196549 - $15.00 USD Received 27 Aug 2013; revised 30 Oct 2013; accepted 20 Nov 2013; published 5 Dec 2013